Heterojunction Annealing Enabling Record Open-Circuit Voltage in Antimony Triselenide Solar Cells

Rong Tang, Shuo Chen, Zhuang-Hao Zheng, Zheng-Hua Su, Jing-Ting Luo, Ping Fan, Xianghua Zhang, Jiang Tang, Guang-Xing Liang

Heterojunction Annealing Enabling Record Open-Circuit Voltage in Antimony Triselenide Solar Cells

*Rong Tang, Shuo Chen, Zhuang-Hao Zheng, Zheng-Hua Su, Jing-Ting Luo, Ping Fan, Xiang-Hua Zhang, Jiang Tang, and Guang-Xing Liang**

Dr. R. Tang, Dr. S. Chen, Prof. Z. H. Zheng, Prof. Z. H. Su, Prof. J. T. Luo, Prof. P. Fan, Prof. G. X. Liang
Shenzhen Key Laboratory of Advanced Thin Films and Applications, Key Laboratory of Optoelectronic Devices and Systems of Ministry of Education and Guangdong Province, College of Physics and Optoelectronic Engineering
Shenzhen University
Shenzhen 518060, P. R. China
E-mail: lgx@szu.edu.cn (Prof. G. X. Liang)
Prof. X. Zhang
CNRS, ISCR (Institut des Sciences Chimiques de Rennes), UMR 6226
Université de Rennes
Rennes F-35000, France
Prof. J. Tang
Wuhan National Laboratory for Optoelectronics (WNLO), School of Optical and Electronic Information
Huazhong University of Science and Technology
Wuhan 430074, P. R. China

Keywords: Sb_2Se_3; Heterojunction; Defect; Open-circuit voltage

Abstract: Despite the fact that antimony triselenide (Sb_2Se_3) thin-film solar cell has undergone rapid development in recent years, the large open-circuit voltage (V_{OC}) deficit still remains to be the biggest bottleneck as even the world record device suffers from a large V_{OC} deficit of 0.59 V. Here, an effective interface engineering approach is reported where the Sb_2Se_3/CdS heterojunction (HTJ) was subjected to a post-annealing treatment using rapid thermal process. It was found that non-radiative recombination near the Sb_2Se_3/CdS HTJ including interface recombination and space charge region recombination were greatly suppressed after the HTJ annealing treatment. Ultimately, a substrate Sb_2Se_3/CdS thin-film solar cell with a competitive power conversion efficiency of 8.64% and a record V_{OC} of 0.52

V has been successfully fabricated. The device exhibits a much mitigated V_{OC} deficit of 0.49 V, which is lower than that of any other reported efficient antimony chalcogenide solar cell.

1. Introduction

Today, the module cost has become a major concern for solar cells and trends are thus moving to thinner and lighter photovoltaic modules. To this end, thin-film technology has seen rapid development over the last few years as chalcogenide solar cells based on $Cu(In,Ga)(S,Se)_2$ (CIGSSe) and CdTe have achieved a power conversion efficiency (PCE) of greater than 22% [1]. Yet the numbers are still far from their respective Shockley-Queisser (SQ) limits, mainly due to severe open-circuit voltage (V_{OC}) losses. Furthermore, the scarcity (In, Ga and Te) and toxicity (Cd) of elements within the light-harvesting compounds might constrain their further employment for mass production. In recent years, more attention was paid to novel semiconducting materials, especially those made from low-toxicity and earth-abundant elements such as Sb_2Se_3, $Cu_2ZnSn(S,Se)_4$ (CZTSSe), GeSe and SnS [2-5].

Among them, antimony triselenide (Sb_2Se_3) has been recognized as a very promising candidate for thin-film photovoltaics in the future. The constituent elements Sb and Se are both low-toxicity and earth-abundant, and hence makes the material suitable for sustainable development. Besides, Sb_2Se_3 has excellent optoelectronic properties with an ideal bandgap (~ 1.2 eV) and high absorption coefficient (> 10^5 cm^{-1}) [2]. The material possesses a unique one-dimensional (1D) crystal structure where $(Sb_4Se_6)_n$ ribbons are covalently bonded in a tilted vertical orientation along which photogenerated carriers are able to travel readily [2]. On the other hand, carrier transport would become much more difficult in horizontal directions since the carriers have to hop between the $(Sb_4Se_6)_n$ ribbons held by van der Waals forces, as demonstrated by Tang's group in 2015 [2]. Due to the strong correlation between the grain orientation and the performance of Sb_2Se_3 solar cell, since then, much effort has

been put into the field of grain orientation control using various thin-film deposition techniques including thermal evaporation, vapor transport deposition (VTD), hydrothermal and sputtering [6-15]. Accordingly, the PCE of Sb_2Se_3 solar cell has increased sharply from 2.1% to 7.6% in only a few years, which was mostly attributed to continuous breakthroughs of the short-circuit current density (J_{SC}) and fill factor (FF) of the device. Mai's group utilized close spaced sublimation (CSS) to prepare [001]-oriented Sb_2Se_3 nanorods which substantially promote the carrier transport within the ribbons [16]. The champion device presented a record PCE of 9.2%, along with significant improved J_{SC} of 32.58 mA/cm^2 and FF of 70.3%, which are 83% and 110% higher than the corresponding parameters of the device with a 2.1% PCE respectively [6]. However, an open-circuit voltage (V_{OC}) of 0.4 V that only showed an 18% enhancement compared to that of the 2.1% PCE device, was still considered as the main bottleneck for the 9.2% champion device. Similarly, other state-of-the-art Sb_2Se_3 solar cells also suffered from an unsatisfied V_{OC} of about 0.4 V [8, 10-12], which is well below the maximum value based on the SQ limit V_{OC}^{SQ} (~0.95 V for a 1.2 eV bandgap). With such a severe V_{OC} deficit (defined as V_{OC}^{SQ} - V_{OC}), the PCE record of Sb_2Se_3 solar cells has stagnated for a few years.

As mentioned above, most of efficient conventional heterojunction (HTJ) thin-film solar cells such as CIGSSe, CdTe and CZTSSe are constrained by V_{OC} deficit to different degrees [1]. In fact, even the well-developed crystalline silicon solar cells are limited by V_{OC} loss as the J_{SC} and FF of the world-record device have almost reached to their SQ limits, whilst there is still plenty of room for the V_{OC} to improve [17]. It goes without saying that the V_{OC} deficit has emerged as the most intractable issue hindering nearly all types of solar cells from further development, particularly for the Sb_2Se_3-based solar cells where excessive V_{OC} deficits (~0.55 V) are often seen for those efficient devices [8, 10-12]. A comprehensive understanding of the origins of V_{OC} deficit would be indispensable to solve the biggest performance bottleneck for

Sb_2Se_3-based solar cells. The V_{OC} deficit causes of Sb_2Se_3 solar cells were extensively studied and can generally be ascribed to two main aspects: First, the free carrier concentration of undoped Sb_2Se_3 is estimated to be ~10^{13} cm^{-3} [19]. This low carrier concentration may limit the built-in voltage V_{bi} which is determined by the carrier concentrations at both the absorber and buffer layers [20], as shown in equation (1)

$$V_{bi} = \frac{k_B T}{q} \ln\left(\frac{N_a N_d}{{n_i}^2}\right) \quad (1)$$

where k_B is the Boltzmann constant, T is the temperature, q is the elementary charge, n_i is the intrinsic carrier concentration, N_a and N_d are the acceptor density and donor density in the Sb_2Se_3 layer and buffer layer, respectively. Since V_{bi} determines the theoretical maximum V_{OC} that the solar cell can exert under illumination, a limited V_{bi} caused by low carrier concentration would primarily lead to V_{OC} loss. Second, abundant defects may exist near the Sb_2Se_3/CdS HTJ including both the interface defects and defects in the space charge region (SCR). These defects, especially those with deep levels, would cause severe recombination near the HTJ, bring band tail states within the bandgap and shorten the carrier lifetime; and therefore, directly contribute to V_{OC} deficit. Despite approaches such as defect engineering of Sb_2Se_3 bulk film [11], buffer layer engineering [10] and back contact optimization [15] have been applied to overcome this main drawback, the general V_{OC} of Sb_2Se_3 solar cells were still rather low.

In this work, the Sb_2Se_3/CdS HTJ was subjected to a post-annealing treatment using rapid thermal process (RTP). Transmission electron microscopy (TEM) revealed the occurrence of substitution of Sb with Cd at the near-surface region of the Sb_2Se_3 absorber due to annealing induced elemental inter-diffusion. The annealing parameters, namely, annealing temperature, chamber pressure, annealing duration and heating rate were carefully studied to better control the elemental inter-diffusion process. It was found that after the HTJ annealing treatment, the doping concentration of the device was considerably increased. Further, the defects near the

HTJ interface especially at the SCR were significantly suppressed. At last, a competitive PCE of 8.64% with a record V_{OC} of 0.52 V were achieved for the champion device.

2. Results and Discussion

The schematic diagram of the Sb_2Se_3 solar cell fabrication is illustrated in Figure 1. A vacuum post-annealing treatment was carried out for the Sb_2Se_3/CdS HTJ once the CdS deposition was finished. The detailed annealing parameters are provided in the Experimental section. It was found that Sb substitution with Cd took place in the $(Sb_4Se_6)_n$ ribbons after the HTJ annealing treatment (Figure 1). For clarity, the devices without and with the HTJ annealing treatment are denoted as untreated device and HTJ-annealed device, respectively in the following text. The *J-V* results are shown in Figure 2a. The untreated device exhibits a V_{OC} of 0.47 V, a J_{SC} of 22.05 mA/cm^2, a FF of 51.8%, and an overall PCE of 5.37%, whilst the corresponding parameters for the HTJ-annealed device were increased to 0.52 V, 27.8 mA/cm^2, 59.8% and 8.64%, respectively after the introduction of the HTJ annealing treatment. The PCE of 8.64% represents the highest efficiency in sputtered-derived Sb_2Se_3 solar cells. The external quantum efficiency (EQE) and corresponding integrated J_{SC} of the two devices are given in Figure 2b, apparently the HTJ-annealed device demonstrates a stronger photoresponse than the untreated device over the whole spectral region. The EQE improvement of the HTJ-annealed device mainly originates from the better photoresponse in the wavelength above 550 nm. The bandgap of the Sb_2Se_3 absorber layers is estimated in the band edge regions by plotting $(E \times \ln(1 - EQE))^2$ versus energy (Figure 2c), which is found to be decreased from 1.33 eV to 1.26 eV after the HTJ annealing treatment. This is predictable since the valence band maximum (VBM) of the Sb_2Se_3 absorber is mainly dominated by s-p hybridization between Sb^{3+} cation and Se^{2-} anion [21], Cd incorporation would induce a stronger p-d hybridization (i.e., Se-4p and Cd-4d) and thus pushing the VBM upward to form a narrower bandgap [22]. Hence, to be more specific, the EQE increase of the

HTJ-annealed device in the wavelength range between 550 nm to 900 nm can be attributed to the reduced non-radiative recombination within the SCR [23], whilst the enhanced photoresponse in the wavelength greater than 900 nm should naturally result from the narrower bandgap owing to the HTJ annealing. Here, it is worth noting that a considerable enlarged V_{OC} (ΔV_{OC} = 50 mV) is exhibited by the HTJ-annealed device with a reduced bandgap compared to the untreated one, implying the significant mitigation of open-circuit voltage deficit ($V_{OC\text{-}def}$) which can be defined as V_{OC}^{SQ} - V_{OC}, where V_{OC}^{SQ} is the theoretical maximum V_{OC} according to the SQ limit that can be calculated using equation (2) [24]:

$$V_{OC}^{SQ} = 0.932 \times E_g - 0.167 \quad (2)$$

where E_g is the bandgap of the absorber. As mentioned before, large V_{OC} deficit has been regarded as the biggest problem that hinders Sb_2Se_3 solar cells from further improvement. Herein, V_{OC} deficits of the state-of-the-art antimony chalcogenide solar cells including Sb_2S_3 and $Sb_2(S,Se)_3$ devices are compared and summarized in Table 1. It can be clearly seen that the $V_{OC\text{-}def}$ of the champion device in this work is much lower than that of any other efficient antimony chalcogenide solar cell reported in the literature, confirming the effectiveness of the HTJ annealing scenario in reducing V_{OC} deficit. Band tailing effects, which usually arise from deep defects at the HTJ interface and within the SCR, are known to be one of the main culprits for the device performance deterioration, especially the large V_{OC} deficit [25]. Urbach energy (E_U) is a measure to evaluate the extents of the band tailing effect which could usually be derived from the EQE data [20, 25, 26]. In this work, E_U of both devices were extracted by plotting ln(-ln(1-EQE)) versus energy (Figure 2d) and a substantial reduction in E_U from 59 meV to 27 meV is observed once the HTJ annealing treatment was applied to the device. Such a dramatic E_U decrease hints that non-radiative recombination near the HTJ region might be greatly reduced possibly due to the deep defect passivation, which will be discussed in more detail later.

TEM characterization was conducted and the cross-sectional image of the whole device is illustrated in Figure 3a. High-angle annular dark-field scanning transmission electron microscope (HAADF-STEM) was further performed at the HTJ interface region and one can note that the Sb_2Se_3/CdS interface is indistinct (Figure 3b), indicating an optimal HTJ interface with less lattice mismatch between the Sb_2Se_3 and CdS. A HAADF-STEM image (the original HAADF-STEM image was Gaussian blur processed to reduce noise level, after which the atomic columns became clearly resolved, as shown in Supplementary Figure S5) with a higher magnification, i.e. 15.5 Mx was taken on the Sb_2Se_3 side approximately 5 nm away from the HTJ interface to scrutinize the atom substitution within the SCR of Sb_2Se_3 (Figure 3c). The atomic structure of the Sb_2Se_3 absorber in this particular region, i.e. [001]-oriented $(Sb_4Se_6)_n$ ribbons in this case, can directly be observed on the atomic scale. The intensity distributions of the HAADF signals are obtained by drawing a profile line across the Sb/Se atoms in atomic columns C1-C5 of the repeat units, as demonstrated in Figure 3d, 3e (atomic columns C1 to C5 are defined in the Supplementary Note 3 and Supplementary Figure S4). The intensity of the HAADF signal is known to be proportional to the mean square of the atomic number *Z* of each atomic column that behaves as a scattering center [27]. Therefore the “bright dots”, displaying strong intensity in Figure 3c can be well assigned to the columns that contain both Sb and Se atoms, namely C1, C2, C4 and C5. These columns with respect to the HAADF signal, are essentially identical regardless of the atom position (see Supplementary Note 3 for detailed explanation). On the other hand, the “dark dots” with much lower intensity, can be assigned to the columns that are occupied by only one Se atoms. For clarity only C1 is selected as representative for atomic columns that contain both Sb and Se atoms. For the untreated device, all the C1 columns display nearly identical intensity (Figure 3e), suggesting the integrity of the repeat units. However, as depicted in Figure 3d, some of the C1 columns show distinct intensity decrease, whose intensities are approximately a third lower than that of other C1 columns but are still much higher than those

of C3 columns. This strongly indicates that after the HTJ annealing treatment, the Sb atoms were substituted by an element whose atomic number falls somewhere in between 34 and 51, which in this case should be Cd. HTJ annealing induced facilitated Cd diffusion from CdS buffer into Sb_2Se_3 absorber occupying the Sb position, forming the Cd_{Sb} antisite at the top Sb_2Se_3 region (SCR), can be directly detected at the atomic scale by such an obvious variation in column intensity.

Energy dispersive spectroscopy (EDS) elemental line scans were then carried out to further study the HTJ annealing effect on elemental distribution of the devices (Figure 3f, 3g). A sharp increase of diffusion length of Cd on the Sb_2Se_3 side can be found after the HTJ annealing, which would certainly facilitate cation substitution. X-ray photoelectron spectroscopy (XPS) elemental depth profiles were carried out as complementary information to the EDS data, as depicted in Supplementary Figure S6. Remarkable Cd diffusion on Sb_2Se_3 side upon HTJ annealing is clearly observed, which is consistent with the EDS results in Figure 3. It is worth noting that promoted elemental diffusion of Sb and Se can also be found on CdS side, with the diffusion extent of Sb being much greater than that of Se. This finding is consistent with Li's report where substantial Sb interdiffusion seemed inevitable at the Sb_2Se_3/CdS interface [16]. In this work we believe the post HTJ annealing at a mediate temperature would accelerate the Sb diffusion to a certain extent, giving rise to Sb depletion in the very top region of Sb_2Se_3 (SCR). Moreover, it is worth mentioning that a considerable promoted S diffusion from CdS into Sb_2Se_3 is also spotted in the EDS results, implying the possibility of anion substitution, i.e. S occupying Se position might not be ruled out. However, S incorporation would normally lead to an enlarged bandgap for pure selenide thin film [28], which contradicts our EQE results before where the Sb_2Se_3 bandgap is found to be smaller after the HTJ annealing. Therefore, a significant Se substitution by S may not be the case in this study. Tang's group reported a blue shift of XRD diffraction peaks after a

Sb_2Se_3/CdS/Sb_2Se_3 structure being subjected to a prolonged annealing treatment (300 °C for 72 h), which suggested Cd interstitial Cd_i, might form at the gap between the $(Sb_4Se_6)_n$ ribbons, contributing to a n-type doping [29]. It is interesting to find out whether these Cd interstitial defects were formed in our case. XRD analyses were firstly undertaken for the pure Sb_2Se_3 thin film and the as-annealed Sb_2Se_3/CdS composite, then the CdS layer was etched away from Sb_2Se_3 using hydrochloric acid (HCl) at a low concentration (approximately 5%) after which the Sb_2Se_3 got tested again. No peak shifting was found for both the as-annealed composite and CdS etched sample (Supplementary Figure S7), suggesting Cd embedding between the $(Sb_4Se_6)_n$ ribbons might not take place in our case most likely due to the short annealing time.

Figure 4 provides the diode properties and capacitance voltage (*C-V*) characterization results of the two devices. The values of these parameters are summarized in Table 2. The decrease of ideality factor *A* from 2.11 to 1.81 suggests recombination suppression in both the HTJ interface and SCR for the annealed device [30]. In addition, a decrease of an order of magnitude in the reverse saturation current density J_0 was also observed for the HTJ-annealed device, confirming the non-radiative recombination has been reduced near the HTJ interface probably due to lower deep defect concentration in this particular region [30]. To verify this, *C-V* profiling and drive-level capacitance profiling (*DLCP*) measurements were then performed (Figure 4d). In the HTJ-annealed device, remarkable increases have been found for both the profiling measurements, and in particular, the *DLCP* curve, which is reported to be more sensitive to free carriers and defect states within the bulk film [8]. We presumably ascribe this prominent increase in *DLCP* to the formation of Cd_{Sb} antisites within the SCR on Sb_2Se_3 side after the HTJ annealing process. These Cd_{Sb} antisites are hole traps that might effectively contribute to p-type doping. According to equation (1), V_{bi} is directly proportional to the natural log of acceptor density N_a and it can be calculated that an increase of an order of

magnitude in N_a could lead to a proximate increase of 60 mV in V_{bi}. The V_{bi} values are obtained as 0.64 V and 0.74 V from the C^{-2}-V plots (Figure 4e) for the untreated device and HTJ-annealed device, respectively. As is well known a large V_{bi} is the prerequisite for high V_{OC}, the improved V_{OC} of the HTJ-annealed device can thereby be attributed, at least partially, to the substantial increase in V_{bi} (ΔV_{bi} = 100 mV).

In principle, *C-V* measurement would contain capacitance responses from free carriers, bulk defects and interface defects, whereas *DLCP* measurement is only sensitive to responses from free carriers and bulk defects. Therefore, the interface defect density could often be calculated from the discrepancy between the *C-V* and *DLCP* profiling at zero bias [8]. The doping densities derived from the *C-V* and DLCP measurements, as well as the estimated interface defect density (N_i) for the two devices are listed in Supplementary Table S1. A notable N_i decrease is found for the HTJ-annealed device, indicating interface defect states mainly originated from lattice mismatch between CdS and Sb_2Se_3, has been reduced after the HTJ annealing treatment. Furthermore, the SCR width (W_d) of the device is decreased from 320 nm to 199 nm after HTJ annealing. This is to some extent predictable since W_d will be shorten with increasing doping density, according to equation (3) as below [31]:

$$W_d = \sqrt{\frac{2\varepsilon_S}{q}\left(\frac{1}{N_a}+\frac{1}{N_d}\right)V_{bi}} \quad (3)$$

where ε_S is permittivity of Sb_2Se_3, q is the elementary charge, N_a and N_d are the acceptor density and donor density in Sb_2Se_3 and CdS, respectively and V_{bi} is the built-in voltage across the PN junction. It is worth pointing out that the SCR is practically acting as an insulation layer where all charge carriers are "depleted" in conventional thin-film solar cells. A too-thick SCR would impair the conductivity of the device and thereby degrade the device performance. Most efficient thin-film chalcogenide devices have a W_d less than 200 nm [12, 20, 32]. The HTJ annealing induced W_d shrinkage of the device in our case reduces the series resistance R_S from 2.7 to 2.3 $\Omega \cdot cm^2$ (Table 2) and thus leading to an improved FF for the

device. In addition, a decreased W_d could also be beneficial for mitigating recombination within the SCR and hence accounting for V_{OC} improvement [33]. Temperature-dependent open-circuit voltage (V_{OC}-T) measurements were carried out to further explore recombination mechanism in the devices. The recombination activation energies E_a of the devices were obtained by extrapolating V_{OC} to the Y-axis, as demonstrated in Figure 4f. The deviation between E_a and E_g of the Sb_2Se_3 absorber is 0.09 eV for the HTJ-annealed device, which is much lower than that of the untreated device (0.3 eV). This is a strong indication that non-radiative recombination in the Sb_2Se_3/CdS interface has been significantly reduced thanks to the HTJ annealing treatment.

Deep-level transient spectroscopy (DLTS) was then applied to investigate the dynamics of defect properties. Figure 5a displays the DLTS signals containing both positive and negative peaks from the two devices. According to literature, the positive peaks and negative peaks can be ascribed to majority carrier traps and minority carrier traps respectively [34]. Consequently, two electron traps and a hole trap, which are denoted as E1, E2 and H1, can be well identified in the untreated device. Interestingly, a new hole trap which is denoted as H2, appears in the HTJ-annealed device. This additional hole trap can almost certainly be associated with the introduction of Cd_{Sb} antisites into $(Sb_4Se_6)_n$ ribbons induced by promoted Cd diffusion via HTJ annealing. The defect characteristics including activation energy (E_T), defect density (N_T) and capture cross-section (σ) are summarized in Table 3. It should be noted that apart from H2 in the HTJ-annealed device, the rest of the defects are all showing very close activation energies in both devices, suggesting they might originate from the same defect categories. Considering the activation energies of these three defect types are in good agreement with the theoretical results from the first-principal calculation in literature [21], E1, E2 and H1 can be well assigned to intrinsic defects of antimony antisite (Sb_{Se}), selenium vacancy (V_{Se}) and selenium antisite (Se_{Sb}), respectively. The defect densities of E1 and E2 in the untreated

device are considerably decreased after HTJ annealing, whilst the corresponding parameters of H1 are increased instead. We attributed this apparent difference in defect dynamics to the promoted elemental interdiffusion induced by HTJ annealing. As discussed earlier, excess Sb diffusion into CdS side due to the annealing would lead to a Sb depletion in the SCR of Sb_2Se_3, making the Sb_2Se_3 surface Sb-poor (Se-rich). In addition, according to our previous reports, the crystallized Sb_2Se_3 films fabricated via the sputtering-selenization technique are usually slightly Sb-rich [14, 35]. The transition from Sb-rich to Sb-poor would increase the formation energies of donor defects such as V_{Se} and Sb_{Se}, resulting in concentration decreases of these defects [21]. In contrast, this transition would lower the formation energy of Se_{Sb}, besides, the dramatic decrease of Sb content on the surface of Sb_2Se_3 could increase Sb vacancy (V_{Sb}) density in this particular region. Some Se atoms are thus very likely to occupy these Sb vacancies to form Se_{Sb} antisites, leading to concentration increase of Se_{Sb}.

The product of the trap density and capture cross-section (denoted as $N_T \times \sigma$) is regarded as a useful index to estimate the device quality for thin-film solar cells [36], since charge trap lifetime (τ_{trap}) is inversely proportional to the value of $N_T \times \sigma$, according to the equation as below [34]:

$$\tau_{trap} = \frac{1}{v\sigma N_T} \quad (4)$$

where v is the mean thermal velocity of charge, σ is the capture cross-section, N_T is the trap density. The values of $N_T \times \sigma$ for each defect category in both devices are listed in Table 3. Figure 5c, 5d illustrate the band edge positions and defect levels for both devices. One can note that E2 (V_{Se}) is located closest to the midgap, being an effective recombination center for both devices. Given for each device E2 also possesses the largest capture cross-section, making it attractive to both electrons and holes. As a result, the photogenerated electrons and holes are prone to be captured by E2 defects and result in severe trap-assisted recombination, leading to significant losses of carrier lifetime and V_{OC}. Further, the E2 defect in untreated

device shows a $N_T \times \sigma$ value much higher than that of other defects. It is reasonable to believe although E1, E2 and H1 whose activation energies are over 500 meV, are all deep defects contributing to trap-assisted recombination, E2 is the main V_{OC}-limiting culprit. After HTJ annealing, the $N_T \times \sigma$ of E1 and H1 are markedly decreased and slightly increased, respectively. More importantly, the corresponding value of E2 has been decreased by over an order of magnitude. The overall decrease in the values of $N_T \times \sigma$ indicates an effective passivation of deep defects within SCR of the device owing to HTJ annealing. Notably, the newly formed H2 (Cd_{Sb}) in the HTJ-annealed device shows a much lower activation energy (243 meV above the VBM) compared to the other three deep defects. The H2 also has a capture cross-section as low as 1.55×10^{-18} cm^2. With such a small capture cross-section, holes will be emitted again in a very short time after they are captured by this shallow state. Moreover, the $N_T \times \sigma$ value of H2 is calculated as 8.23×10^{-4} cm^{-1}, which is comparable to those of high-quality perovskite solar cells [36]. For this reason, H2 will unlikely act as a recombination center diminishing carrier lifetime and V_{OC}. Instead, it might be a shallow acceptor contributing to effective p-type doping and thus V_{bi} enlargement of the device. This is also evidenced by the downshift and upshift of the Fermi level and VBM, respectively in the HTJ-annealed device (Figure 5d). Under illumination, photogenerated electrons and holes would be swept into CdS and Sb_2Se_3 sides driven by electric field within the SCR, making the electron quasi-Fermi level (E_{Fn}) and hole quasi-Fermi level (E_{Fp}) move upward and downward in CdS and Sb_2Se_3 layers respectively. The ultimate V_{OC} is determined by the split of the two quasi-Fermi levels of electrons and holes. In the untreated device, the E_{Fp} is prone to be pinned near to the midgap due to the large amount of deep defect E2 and resulted in a limited V_{OC} under illumination, as depicted in Figure 5e. Passivation of these detrimental defects via the HTJ annealing process could alleviate the E_{Fp} pinning effect and boost the split of the two quasi-Fermi levels of electrons and holes, leading to an enlarged V_{OC} for the device.

To monitor the carrier transport dynamics for the untreated and HTJ-annealed Sb_2Se_3 absorber films, transient absorption spectroscopy (TAS) was applied. Prior to TAS characterization, the CdS films were etched way from both the untreated and HTJ-annealed Sb_2Se_3/CdS layered structures that were deposited on soda-lime glass. A distinct photo-induced absorption (PIA) peak at 720 nm is observed for both samples (Figure 5e), which can be assigned to trapping of photogenerated minority carrier (electron) in the Sb_2Se_3 absorber films. Hence, the transient kinetic decay of the PIA peak at 720 nm are fitted by a biexponential model (Figure 5f) containing a short decay (τ_1) and a long decay (τ_2) lifetime. The short decay and long decay components can be well assigned to the interface/surface recombination and the bulk defect recombination, respectively [30]. The fitting parameters are summarized in Supplementary Table S2. Both the lifetime components are increased after HTJ annealing with the increasing rate of the long decay lifetime (from 880 ps to 5721 ps) being much higher than that of the short decay lifetime (from 110 ps to 234 ps). As a result, a far superior overall lifetime (τ = 5662 ps) of photogenerated minority carrier was obtained for the HTJ-annealed sample, being one of the top values among those highly efficient Sb_2Se_3 thin-film solar cells [11, 37]. This indicates that both interface/surface recombination and bulk recombination within the device have been suppressed after HTJ annealing, along with the bulk recombination mitigation playing as a more dominant role. This finding echoes the results from the diode characterization and V_{OC}-T measurements. We attribute this sharp increase of the long decay lifetime to effective passivation of deep defects with large capture cross-section, which would mostly occur in the SCR of Sb_2Se_3 absorber film where the element interdiffusion take place due to HTJ annealing. The prolonged lifetime of photogenerated minority carrier would eventually result in V_{OC} improvement of the device.

3. Conclusions

In this work, aiming to mitigate the main limitation of V_{OC} deficit for Sb_2Se_3-based thin-film solar cells, we have demonstrated an effective interface engineering scenario where the Sb_2Se_3/CdS HTJ was subjected to a post-annealing treatment at a mediate temperature using RTP technique. Sb substitution by Cd induced by promoted elemental interdiffusion could be directly revealed by the TEM characterization at the near-surface region of the Sb_2Se_3 absorber. The doping concentration of the device has been increased after HTJ annealing due to the occurrence of the shallow Cd_{Sb} hole traps. Additionally, deep defects within the SCR of Sb_2Se_3 have been passivated after HTJ annealing. Consequently, non-radiative recombination near the Sb_2Se_3/CdS HTJ including interface recombination and SCR recombination were suppressed, leading to an extended minority lifetime of the device. The 8.64% PCE of the champion device represents the highest value for sputtered Sb_2Se_3 devices and a record V_{OC} of 0.52 V has been achieved for all Sb_2Se_3 thin-film solar cells by far. Meanwhile, the device exhibits a much mitigated V_{OC} deficit of 0.49 V, which is the lowest among all efficient antimony chalcogenide solar cells.

4. Experimental Section

Preparation of Sb_2Se_3 and CdS thin films

Sb metallic precursors were deposited using a radiofrequency (RF) magnetron sputtering deposition system. Mo-coated glass substrates were subsequently cleaned in an ultrasonic bath using detergent, ethanol, and deionized water before sputtering deposition. The background pressure of the sputtering vacuum chamber was evacuated below 5.0×10^{-4} Pa before the sputtering procedure commenced. High-purity (>99.999%) Ar gas was introduced into the sputtering chamber at a flow rate of 40 sccm. The working pressure and sputtering power were kept at 1.0 Pa and 35 W during the sputtering process, respectively. The sputtering duration was 40 min without additional in-situ heat treatment to obtain Sb metallic precursor with thickness of approximately 700 nm.

Once the sputtering process was finished, the as-sputtered Sb precursors and 0.2 g of high-purity (>99.99%) selenium (Se) powder were separately placed into the two chambers of a vacuum tubular furnace for selenization. The chambers were evacuated using a mechanical pump before introducing high-purity Ar gas. During the annealing process, the Se powder side temperature and the Sb precursor side temperature were ramped up to 400 °C and 410 °C, respectively at a heating rate of 20 °C/min. The working pressure was kept at 5×10^4 Pa and the selenization duration was 15 min. The furnace was naturally cooled down to room temperature when the heating process was finished.

CdS buffer layer was deposited onto the crystallized Sb_2Se_3 thin films using chemical bath deposition (CBD) after selenization. $CdSO_4$ aqueous solution (0.015 M, 20 mL), thiourea aqueous solution (0.75 M, 20 mL) and ammonium hydroxide aqueous solution (14.8 M, 20 mL) were subsequently added to deionized water (140 mL). The substrates were soaked into the mixed solution which was then placed in an 80 °C water bath under continuous stirring for 9 min.

Sb_2Se_3/CdS heterojunction (HTJ) post-annealing treatment

After the deposition of CdS buffer layer, the film was blow-dried using N_2 jet. Subsequently, the film was placed into a vacuum tubular furnace. The tubular furnace was evacuated to a background pressure of 10 Pa before the heating process started. After that the furnace temperature was raised to 300 °C within 10 seconds and then kept at 300 °C for 120 seconds. The sample was pulled out immediately from the furnace using a slide rail once the heating program was finished. The ambient temperature and relative humidity were 25±2°C and 55±10%, respectively.

Device fabrication

ITO thin films were then magnetron sputtered onto the Sb_2Se_3/CdS structure as a window layer. The device surface was scribed into small squares with identical area by knife and Ag electrodes were deposited onto the ITO surface via thermal evaporation to form metallic contact. A substrate configuration of Mo/Sb_2Se_3/CdS/ITO/Ag was assembled for our Sb_2Se_3 solar cells. The active area of each device is 0.14 cm^2.

Thin film characterization

A scanning electron microscope (SEM, SUPRA 55) was utilized to study the top-view and cross-sectional microstructure of the Sb_2Se_3 thin films. The film orientation was studied by X-ray diffraction (XRD, Ultima-iv, CuK_α radiation under operation conditions of 40 kV and 40 mA from 10° to 60°). Transmission electron microscope (TEM) images were taken using a FEI Titan Cubed Themis G2 300 microscope. The samples for TEM imaging were prepared by ablating the device using focused ion beam (FIB, FEI Scios). Ultraviolet photoelectron spectroscopy (UPS) and x-ray photoelectron spectroscopy (XPS) measurements were carried out using an ultraviolet photoemission spectrometer and an X-ray photoelectron spectrometer (Thermo Scientific ESCALAB 250Xi). Elemental depth profiling was obtained by sputtering the surface of CdS/Sb_2Se_3 with 1keV Ar^+ ions over an etching area of 2.5×2.5 mm^2. Transient absorption spectroscopy (TAS) spectra were measured using a transient absorption spectrometer (Newport) which was equipped with a Spectra-Physics Solstice Ace regenerative amplifier (800 nm wavelength, 100 fs pulses with 1 kHz repetition rate). The decay characteristics were fitted by a biexponential model $y = \sum A_i \exp(-x/t_i)$.

Device characterization

The current density-voltage (*J-V*) curves of the devices were measured under 100 mW/cm^2 AM 1.5 G light illumination using a class AAA solar simulator at room temperature. The external quantum efficiency (EQE) curves were measured using a Zolix SCS101 system and a Keithley 2400 source meter. Capacitance-voltage (*C-V*) measurements were performed at AC

amplitude of 30 mV and frequency of 10 kHz under dark condition at room temperature. Temperature-dependent V_{OC} measurements were conducted using a Lakeshore 325 temperature controller and the temperature was swept from 350 K to 120 K. The devices were mounted inside a Janis VPF-100 cryostat and cooled with liquid nitrogen during the measurements. The deep-level transient spectroscopy (DLTS) spectra were obtained using an FT-1030 HERA DLTS system equipped with a Janis VPF-800 cryostat controller.

Supporting Information

Supporting Information is available from the Wiley Online Library or from the author.

Acknowledgements

R.T. and S.C. contributed equally to this work. This work was supported by National Natural Science Foundation of China (No. 62074102, 62104157 and 62104156), Key Project of Department of Education of Guangdong Province (No. 2018KZDXM059), Science and Technology plan project of Shenzhen (JCYJ20190808153409238). The authors wish to acknowledge the assistance on HAADF-STEM observation received from the Electron Microscope Center of the Shenzhen University. Thanks for Prof. Zhi-Qiang Li's assistance on XPS and UPS. Thanks for Li-Jing Wang's help on DLTS. Thanks for Dr Ayyaz Mahmood's help on crystal structure drawing. Thanks for Jun-Zi Li's help on TAS.

Author Contributions

G.L. supervised the project. R.T. and S.C. contributed equally to this work. G.L. and R.T. conceived the original concept and designed the experiments. R.T. and S.C. fabricated the devices and conducted the photovoltaic characterizations. Z.Z. assisted with the TEM measurement and analysis. Z.S. aided in XPS analysis. J.L., P.F., and X.Z. participated in data analysis. J.T. helped with the manuscript preparation and analysis. R.T., S.C. and G.L. wrote the paper, all the authors commented on the manuscript.

Conflicts of Interest

There are no conflicts to declare.

Data Availability Statement

The original data in this work is available from the corresponding authors upon reasonable request.

Received: ((will be filled in by the editorial staff))
Revised: ((will be filled in by the editorial staff))
Published online: ((will be filled in by the editorial staff))

References

[1] M. A. Green, E. Dunlop, J. Hohl-Ebinger, M. Yoshita, N. Kopidakis, X. J. Hao, *Progress. Photovolt. Res. Appl.* **2021**, *29*, 3.

[2] Y. Zhou, L. Wang, S. Y. Chen, S. K. Qin, X. S. Liu, J. Chen, D. J. Xue, M. Luo, Y. Z. Cao, Y. B. Cheng, E. H. Sargent, J. Tang, *Nat. Photon.* **2015**, *9*, 409.

[3] W. Wang, M. T. Winkler, O. Gunawan, T. Gokmen, T. K. Todorov, Y. Zhu, D. B. Mitzi, *Adv. Energy Mater.* **2014**, *4*, 1301465.

[4] D. J. Xue, S. C. Liu, C. M. Dai, S. Y. Chen, C. He, L. Zhao, J. S. Hu, L. J. Wan, *J. Am. Chem. Soc.* **2017**, *139*, 958.

[5] H. S. Yun, B. W. Park, Y. C. Choi, J. Im, T. J. Shin, S. I. Seok, *Adv. Energy Mater.* **2019**, *9*, 1901343.

[6] X. S. Liu, J. Chen, M. Luo, M. Y. Leng, Z. Xia, Y. Zhou, S. K. Qin, D. J. Xue, L. Lv, H. Huang, D. M. Niu, J. Tang, *ACS Appl. Mater. Interfaces* **2014**, *6*, 10687.

[7] K. Shen, C. Z. Ou, T. L. Huang, H. B. Zhu, J. J. Li, Z. Q. Li, Y. H. Mai, *Sol. Energy Mater. Sol. Cells* **2018**, *186*, 58.

[8] L. Wang, D. B. Li, K. H. Li, C. Chen, H. X. Deng, L. Gao, Y. Zhao, F. Jiang, L. Y. Li, F. Huang, Y. S. He, H. S. Song, G. D. Niu, J. Tang, *Nat. Energy* **2017**, *2*, 17046.

[9] X. B. Hu, J. H. Tao, S. M. Chen, J. J. Xue, G. E. Weng, K. Jiang, Z. G. Hu, J. C. Jiang, S. Q. Chen, Z. Q. Zhu, J. H. Chu, *Sol. Energy Mater. Sol. Cells* **2018**, *187*, 170.

[10] J. H. Tao, X. B. Hu, Y. X. Guo, J. Hong, K. H. Li, J. C. Jiang, S. Q. Chen, C. B. Jing, F. Y. Yue, P. X. Yang, C. J. Zhang, Z. C. Wu, J. Tang, J. H. Chu, *Nano energy* **2019**, *60*, 802.

[11] X. X. Wen, C. Chen, S. C. Lu, K. H. Li, R. Kondrotas, Y. Zhao, W. H. Chen, L. Gao, C. Wang, J. Zhang, G. D. Niu, J. Tang, *Nat. Commun.* **2018**, *9*, 2179.

[12] K. H. Li, C. Chen, S. C. Lu, C. Wang, S. Y. Wang, Y. Lu, J. Tang, *Adv. Mater.* **2019**, *31*, 1903914.

[13] D. Liu, R. F. Tang, Y. Y. Ma, C. H. Jiang, W. T. Lian, G. Li, W. H. Han, C. F. Zhu, T.

Chen, *ACS Appl. Mater. Interfaces* **2021**, *13*, 18856.

[14] R. Tang, Z. H. Zheng, Z. H. Su, X. J. Li, Y. D. Wei, X. H. Zhang, Y. Q. Fu, J. T. Luo, P. Fan, G. X. Liang, *Nano Energy* **2019**, *64*, 103929.

[15] Z. Q. Li, X. Chen, H. B. Zhu, J. W. Chen, Y. T. Guo, C. Zhang, W. Zhang, X. N. Niu, Y. H. Mai, *Sol. Energy Mater. Sol. Cells* **2017**, *161*, 190.

[16] Z. Q. Li, X. Y. Liang, G. Li, H. X. Liu, H. Y. Zhang, J. X. Guo, J. W. Chen, K. Shen, X. Y. San, W. Yu, R. E. I. Schropp, Y. H. Mai, *Nat. Commun.* **2019**, *10*, 125.

[17] K. Yoshikawa, H. Kawasaki, W. Yoshida, T. Irie, K. Konishi, K. Nakano, T. Uto, D. Adachi, M. Kanematsu, H. Uzu, K. Yamamoto, *Nat. Energy* **2017**, *2*, 1.

[18] K. Shen, Z. Z. Bai, Y. Deng, R. L. Yang, D. Z. Wang, Q. Li, D. L. Wang, *RSC Adv.* **2016**, *6*, 52326.

[19] C. Chen, L. Wang, L. Gao, D. Nam, D. B. Li, K. H. Li, Y. Zhao, C. Ge, H. Cheong, H. Liu, H. S. Song, J. Tang, *ACS Energy Lett.* **2017**, *2*, 2125.

[20] Z. H. Su, G. X. Liang, P. Fan, J. T. Luo, Z. H. Zheng, Z. G. Xie, W. Wang, S. Chen, J. G. Hu, Y. D. Wei, C. Yan, J. L. Huang, X. J. Hao, F. Y. Liu, *Adv. Mater.* **2020**, *32*, 2000121.

[21] M. L. Huang, P. Xu, D. Han, J. Tang, S. Y. Chen, *ACS Appl. Mater. Interfaces* **2019**, *11*, 15564.

[22] S. H. Wei, A. Zunger, *Appl. Phys. Lett.* **1998**, *72*, 2011-2013.

[23] Z. H. Su, K. W. Sun, Z. L. Han, H. T. Cui, F. Y. Liu, Y. Q. Lai, J. Li, X. J Hao, Y. X. Liu, M. A. Green, *J. Mater. Chem. A* **2014**, *2*, 500.

[24] A. D. Collard, H. W. Hillhouse, *Chem. Mater.* **2016**, *28*, 2067.

[25] Y. C. Gong, R. C. Qiu, C. Y. Niu, J. J. Fu, E. Jedlicka, R. Giridharagopal, Q. Zhu, Y. G. Zhou, W. B. Yan, S. T. Yu, *Adv. Funct. Mater.* **2021**, 2101927.

[26] Y. C. Gong, Y. F. Zhang, Q. Zhu, Y. G. Zhou, R. C. Qiu, C. Y. Niu, W. B. Yan, W. Huang, H. Xin, *Energy Environ. Sci.* **2021**, *14*, 2369-2380

[27] B. Rafferty, P. D. Nellist, S. J. Pennycook, **2001**, *50*, 227.

[28] R. F. Tang, X. M. Wang, W. T. Lian, J. L. Huang, Q. Wei, M. L. Huang, Y. W. Yin, C. H. Jiang, S. F. Yang, G. C. Xing, S. Y. Chen, C. F. Zhu, X. J. Hao, M. A. Green, T. Chen, *Nat. Energy* **2020**, *5*, 587.

[29] Y. Zhou, Y. Li, J. J. Luo, D. B. Li, X. S. Liu, C. Chen, H. B. Song, J. Y. Ma, D. J. Xue, B. Yang, J. Tang, *Appl. Phys. Lett.* **2017**, *111*, 013901.

[30] C. Chen, J. Tang, *ACS Energy Lett.* **2020**, *5*, 2294.

[31] J. A. Nelson, *The physics of solar cells.* World Scientific Publishing Company, **2003**.

[32] C. Yan, J. L. Huang, K. W. Sun, S. Johnston, Y. F. Zhang, H. Sun, A. B. Pu, M. R. He, F.

Y. Liu, K. Eder, L. M. Yang, J. M. Cairney, N. J. Ekins-Daukes, Z. Hameiri, J. A. Stride, S. Y. Chen, M. A. Green, X. J. Hao, *Nat. Energy* **2018**, *3*, 764.

[33] X. Niu, H. Zhu, X. Liang, Y. Guo, Z. Li, Y. Mai, *Appl. Surf. Sci.* **2017**, *426*, 1213.

[34] W. T. Lian, C. H. Jiang, Y. W. Yin, R. F. Tang, G. Li, L. J. Zhang, B. Che, T. Chen, *Nat. Commun.* **2021**, *12*, 1.

[35] Y. D. Luo, R. Tang, S. Chen, J. G. Hu, Y. K. Liu, Y. F. Li, X. S. Liu, Z. H. Zheng, Z. H. Su, X. F. Ma, P. Fan, X. H. Zhang, H. L. Ma, Z. G. Chen, G. X. Liang, *Chem. Eng. J.* **2020**, *393*, 124599.

[36] A. A. B. Baloch, M. I. Hossain, N. Tabet, F. H. Alharbi, *J. Phys. Chem. Lett.* **2018**, *9*, 426.

[37] Y. Ma, B. Tang, W. Lian, C. Wu, X. Wang, H. Ju, C. Zhu, F. Fan, T. Chen, J. Mater. Chem. A **2020**, *8*, 6510.

[38] X. M. Wang, R. F. Tang, C. H. Jiang, W. T. Lian, H. X. Ju, G. S. Jiang, Z. Q. Li, C. F. Zhu, T. Chen, *Adv. Energy Mater.* **2020**, *10*, 2002341.

[39] C. H. Jiang, J. Zhou, R. F. Tang, W. T. Lian, X. M. Wang, X. Y. Lei, H. L. Zeng, C. F. Zhu, W. H. Tang, T. Chen, *Energy Environ. Sci.* **2021**, *14*, 359-364.

[40] Y. C. Choi, D. U. Lee, J. H. Noh, E. K. Kim, S. I. Seok, *Adv. Funct. Mater.* **2014**, *24*, 3587.

[41] T. Liu, X. Y. Liang, Y. F. Liu, X. L. Li, S. F. Wang, Y. H. Mai, Z. Q. Li, *Adv. Sci.* **2021**, 2100868.

Table 1. Summary of V_{OC} deficits of the state-of-the-art antimony chalcogenide solar cells.

Materials	PCE (%)	V_{OC} (V)	E_g (eV)	V_{OC}^{SQ} (V)	$V_{OC\text{-}def}$ (V)	Ref.
$Sb_2(S,Se)_3$	10.0	0.63	1.49	1.22	0.59	Chen [28]
	10.5	0.664	1.55	1.28	0.614	Chen [38]
	9.7	0.634	1.5	1.23	0.596	Chen [39]
Sb_2S_3	7.5	0.711	1.77*	1.48	0.769	Seok [40]
	6.2	0.72	1.7	1.42	0.7	Chen [34]
Sb_2Se_3	9.2	0.4	1.24	0.99	0.59	Mai [16]
	9.19	0.461	1.24	0.99	0.529	Li [41]
	7.62	0.386	1.21*	0.96	0.574	Tang [12]
	7.6	0.42	1.19	0.94	0.52	Tang [11]
	7.89	0.449	1.23	0.98	0.53	Chen [13]
	8.64	**0.52**	**1.26**	**1.01**	**0.49**	**This work**

Note: The E_g value with the mark * were not provided directly by the authors and are estimated from the EQE results

Table 2. The photovoltaic and diode parameters of the untreated and HTJ-annealed device.

Device	V_{OC} (V)	J_{SC} (mA/cm^2)	FF (%)	PCE (%)	R_S (Ω·cm^2)	A	J_0 (A/cm^2)	V_{bi} (V)
Untreated	0.47	22.05	51.8	5.37	2.7	2.11	2.4×10^{-2}	0.64
Annealed	0.52	27.8	59.8	8.64	2.3	1.81	3×10^{-3}	0.74

Table 3. Defect characteristics of the two devices.

Devices	Defects	E_T (eV)	N_T (cm^{-3})	σ (cm^2)	$N_T\times\sigma$ (cm^{-1})
Untreated	E1	$E_C - 0.533$	1.72×10^{14}	1.58×10^{-15}	2.72×10^{-1}
	E2	$E_C - 0.745$	9.3×10^{13}	2.83×10^{-14}	2.63
	H1	$E_V + 0.523$	2.56×10^{14}	9.91×10^{-16}	2.54×10^{-1}
Annealed	E1	$E_C - 0.509$	6.15×10^{13}	5.77×10^{-16}	3.55×10^{-2}
	E2	$E_C - 0.718$	4.7×10^{13}	5.28×10^{-15}	2.48×10^{-1}
	H1	$E_V + 0.534$	4.81×10^{14}	1.39×10^{-15}	6.69×10^{-1}
	H2	$E_V + 0.243$	5.31×10^{14}	1.55×10^{-18}	8.23×10^{-4}

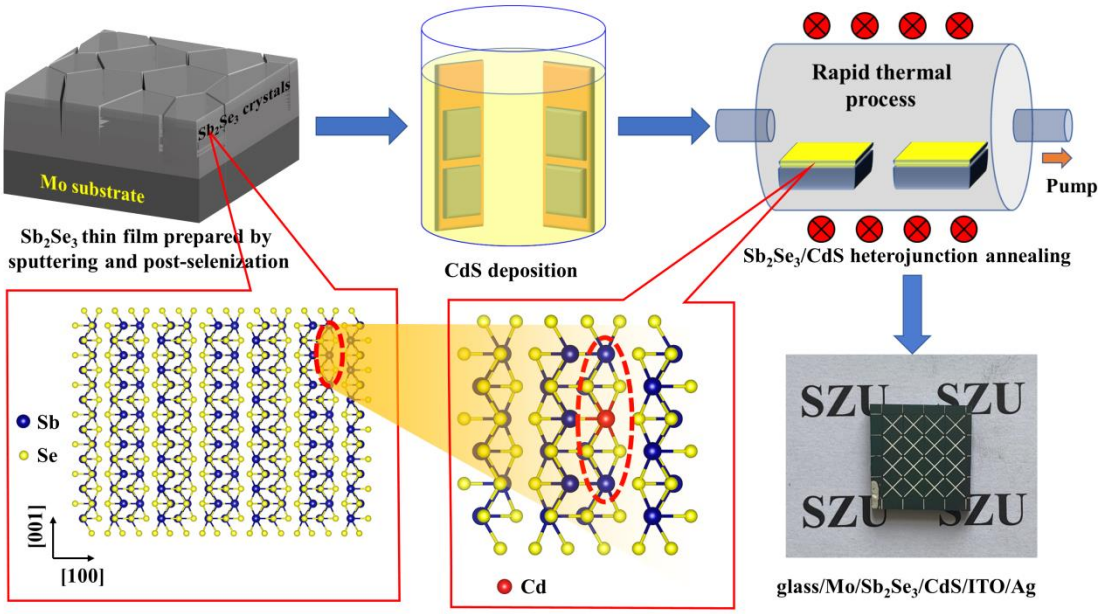

Figure 1. Schematic diagram of the device fabrication process.

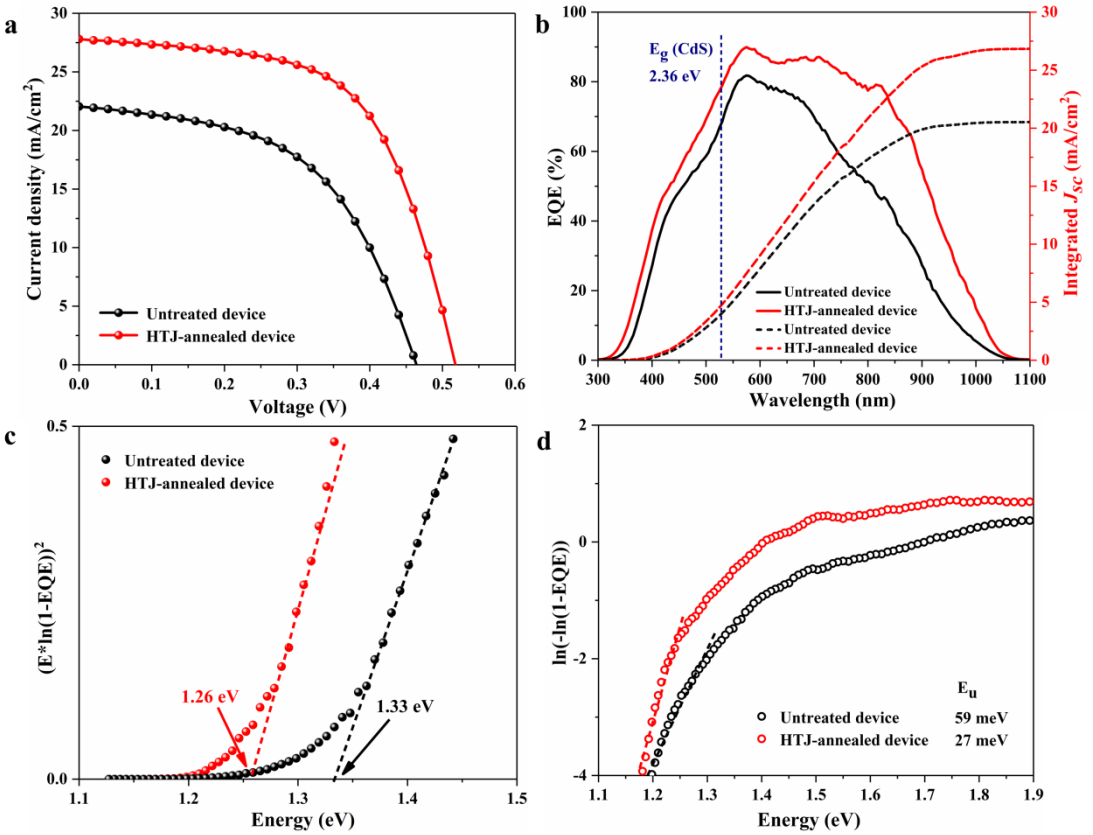

Figure 2. Photovoltaic performance of devices. a *J-V* curves of devices, **b** EQE and integrated J_{SC} of devices, **c** Bandgap derived from the EQE data of devices, **d** Urbach energy derived from the EQE data of devices.

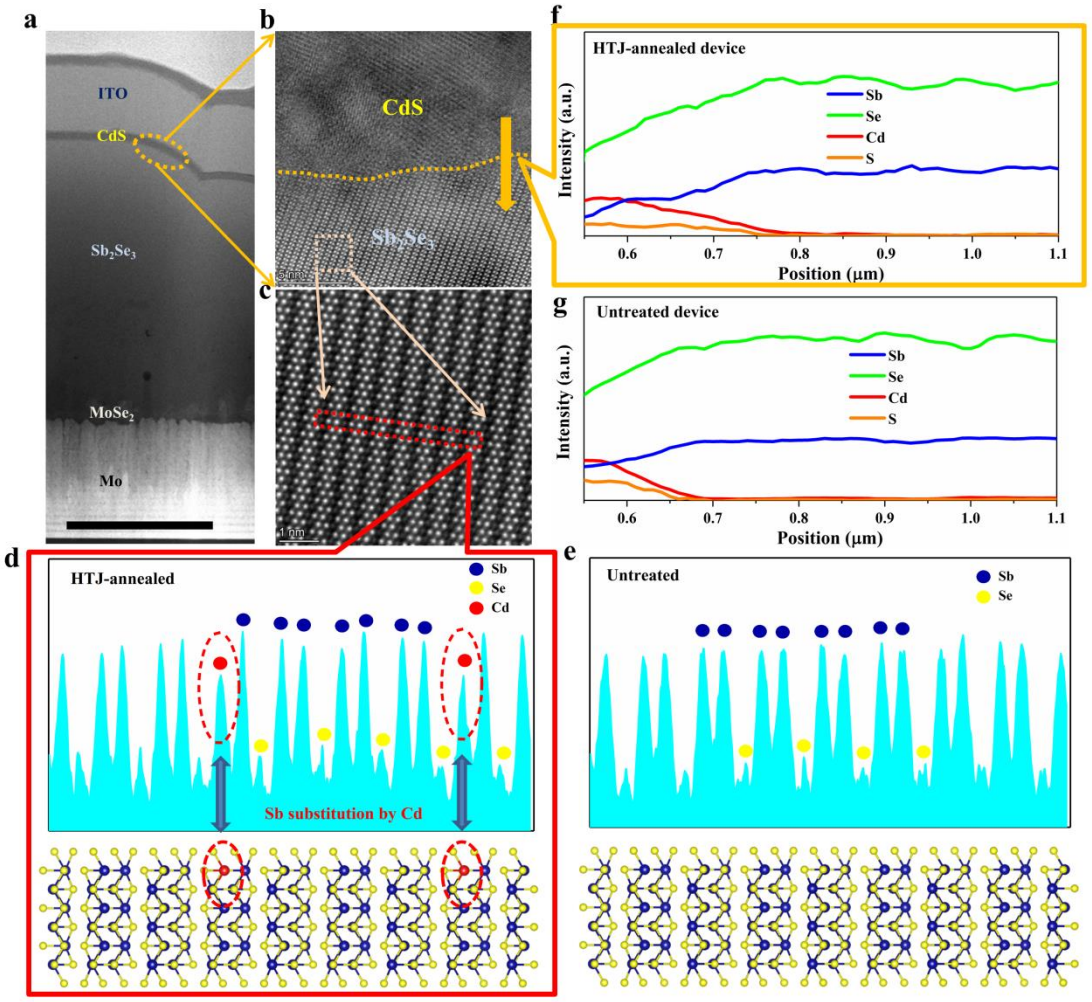

Figure 3. TEM characterization of the HTJ-annealed device. a Cross-sectional TEM image of the HTJ-annealed device. The black scale bar at the bottom of the image reads 1 μm. **b** HAADF-STEM image (magnification: 5.5 Mx) taken at the Sb_2Se_3/CdS interface. **c** HAADF-STEM image (with Gaussian blur processed, magnification: 15.5 Mx) taken at the Sb_2Se_3 side about 5 nm away from the HTJ interface. **d**, **e** The intensity profiles of the HAADF signals in the red dotted box of the HTJ-annealed device and untreated device demonstrating the cation substitution induced by the HTJ annealing. **f**, **g** EDS elemental line scan profiles across the Sb_2Se_3/CdS interfaces of the HTJ-annealed device and untreated device. The orange arrow in Fig. 3b indicates the EDS line scan direction.

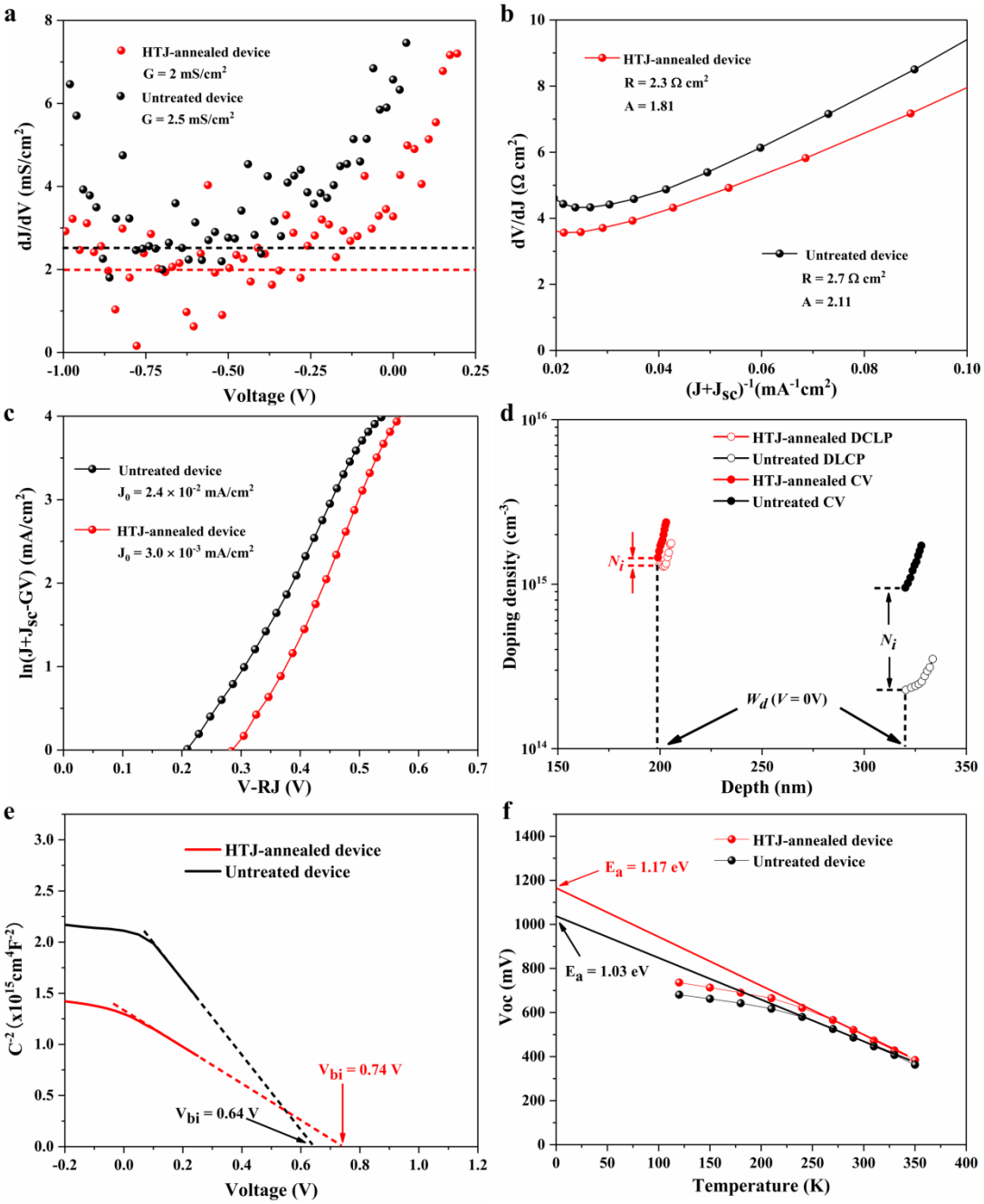

Figure 4. Diode parameters and *C-V* characterization of devices. a Conductance *G*, **b** Series resistance R_S and ideality factor *A*, **c** Reverse saturation current density J_0, **d** *C-V* and *DLCP* profiling, **e** V_{bi} derived from the *C-V* characterization, **f** $V_{OC} - T$ measurements.

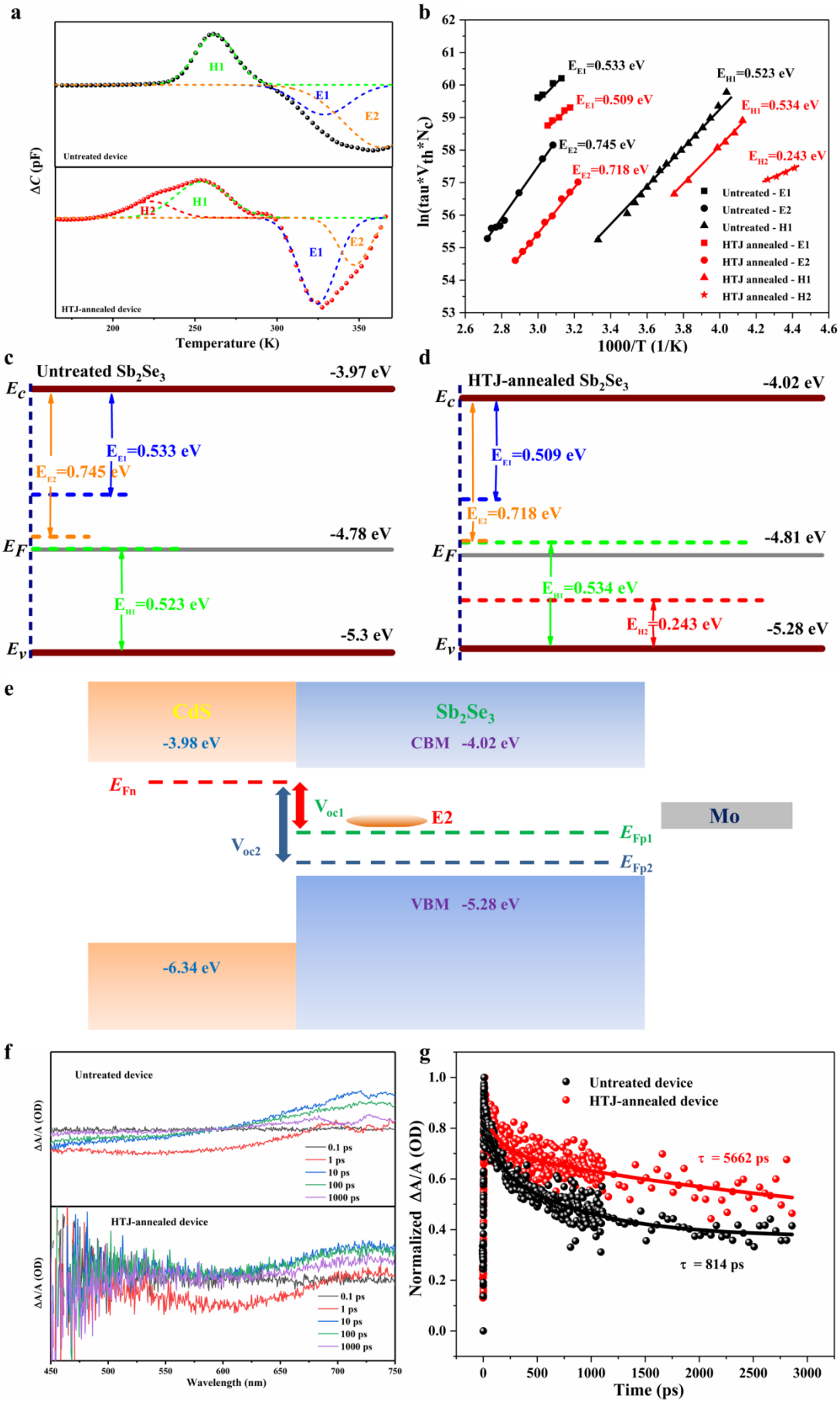
a
H1
E1
E2
Untreated device
H2
H1
E1
E2
HTJ-annealed device
ΔC (pF)
Temperature (K)
b
E_E1=0.533 eV
E_E1=0.509 eV
E_E2=0.745 eV
E_E2=0.718 eV
E_H1=0.523 eV
E_H1=0.534 eV
E_H2=0.243 eV
Untreated - E1
Untreated - E2
Untreated - H1
HTJ annealed - E1
HTJ annealed - E2
HTJ annealed - H1
HTJ annealed - H2
ln(tau*Vth*Nc)
1000/T (1/K)
c
Untreated Sb2Se3
-3.97 eV
Ec
E_E1=0.533 eV
E_E2=0.745 eV
-4.78 eV
EF
E_H1=0.523 eV
-5.3 eV
Ev
d
HTJ-annealed Sb2Se3
-4.02 eV
Ec
E_E1=0.509 eV
E_E2=0.718 eV
-4.81 eV
EF
E_H1=0.534 eV
E_H2=0.243 eV
-5.28 eV
Ev
e
CdS
-3.98 eV
Sb2Se3
CBM -4.02 eV
E_Fn
V_oc1
E2
Mo
E_Fp1
V_oc2
E_Fp2
VBM -5.28 eV
-6.34 eV
f
Untreated device
ΔA/A (OD)
0.1 ps
1 ps
10 ps
100 ps
1000 ps
HTJ-annealed device
ΔA/A (OD)
0.1 ps
1 ps
10 ps
100 ps
1000 ps
Wavelength (nm)
g
Untreated device
HTJ-annealed device
τ = 5662 ps
τ = 814 ps
Normalized ΔA/A (OD)
Time (ps)

Figure 5. DLTS and TAS characterizations of the untreated and HTJ-annealed Sb_2Se_3 films. a DLTS signals from the untreated and HTJ-annealed device. **b** Arrhenius plots obtained from DLTS signals. **c, d** Valence and conduction band positions, Fermi levels and defect levels of the untreated and HTJ-annealed Sb_2Se_3. **e** Schematic diagram of V_{OC} determined by the split of quasi-Fermi levels of electrons and holes under illumination. **f** Time-resolved absorption spectra obtained at various time delays of both films after photoexcitation. **g** Transient kinetic traces of the decay of the PIA peak at 720 nm of both films.

Table of contents: A heterojunction post-annealing treatment was utilized to suppress the non-radiative recombination for a highly competitive power conversion efficiency of 8.64% and a record open-circuit voltage (V_{OC}) of 520 mV in Sb_2Se_3 thin-film solar cells. The V_{OC} deficit of the device is lower than that of any other reported efficient antimony chalcogenide solar cells.

*Rong Tang, Shuo Chen, Zhuang-Hao Zheng, Zheng-Hua Su, Jing-Ting Luo, Ping Fan, Xiang-Hua Zhang, Jiang Tang, and Guang-Xing Liang**

Title: Heterojunction Annealing Enabling Record Open-Circuit Voltage in Antimony Triselenide Solar Cells

ToC figure

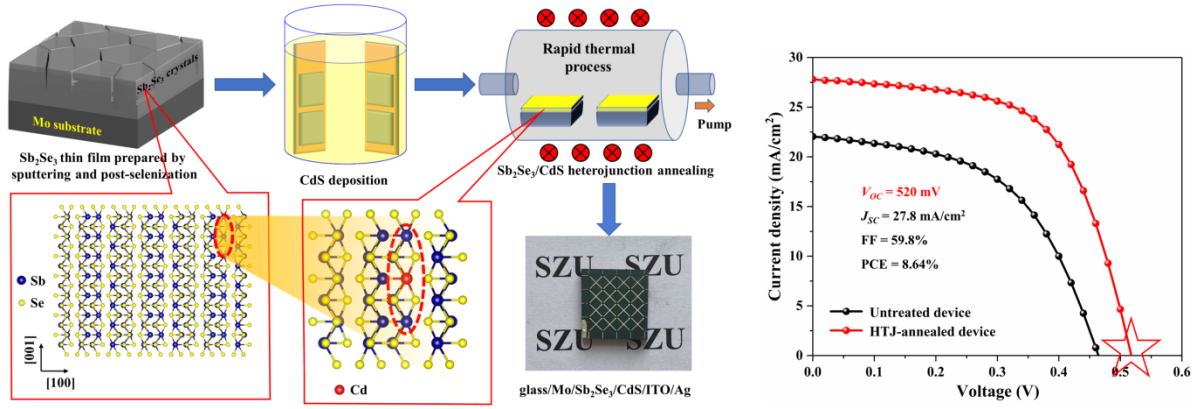

Supporting Information

Heterojunction Annealing Enabling Record Open-Circuit Voltage in Antimony Triselenide Solar Cells

*Rong Tang, Shuo Chen, Zhuang-Hao Zheng, Zheng-Hua Su, Jing-Ting Luo, Ping Fan, Xiang-Hua Zhang, Jiang Tang, and Guang-Xing Liang**

Dr. R. Tang, Dr. S. Chen, Prof. Z. H. Zheng, Prof. Z. H. Su, Prof. J. T. Luo, Prof. P. Fan, Prof. G. X. Liang
Shenzhen Key Laboratory of Advanced Thin Films and Applications, Key Laboratory of Optoelectronic Devices and Systems of Ministry of Education and Guangdong Province, College of Physics and Optoelectronic Engineering
Shenzhen University
Shenzhen 518060, P. R. China
E-mail: lgx@szu.edu.cn (Prof. G. X. Liang)
Prof. X. Zhang
CNRS, ISCR (Institut des Sciences Chimiques de Rennes), UMR 6226
Université de Rennes
Rennes F-35000, France
Prof. J. Tang
Wuhan National Laboratory for Optoelectronics (WNLO), School of Optical and Electronic Information
Huazhong University of Science and Technology
Wuhan 430074, P. R. China

Supplementary Note 1

The morphology of the as-prepared Sb_2Se_3 thin film was studied by scanning electron microscope (SEM) and X-ray diffraction (XRD), the corresponding results are provided in Supplementary Figure S1. Large Sb_2Se_3 grains with size over 1 μm are clearly observed from both the SEM top-view and cross-sectional images. The average thickness of the crystallized Sb_2Se_3 film was estimated to be 1.5 μm (Supplementary Figure S1c). The Sb_2Se_3 grains demonstrate a quasi-vertical orientation, as indicated by the strong (211), (221) and (002) diffraction peaks of the XRD spectrum. These large-sized, crack-free and vertically oriented grains are essential to facilitate carrier transport within the light harvesting layer and are the prerequisite for efficient Sb_2Se_3 device.

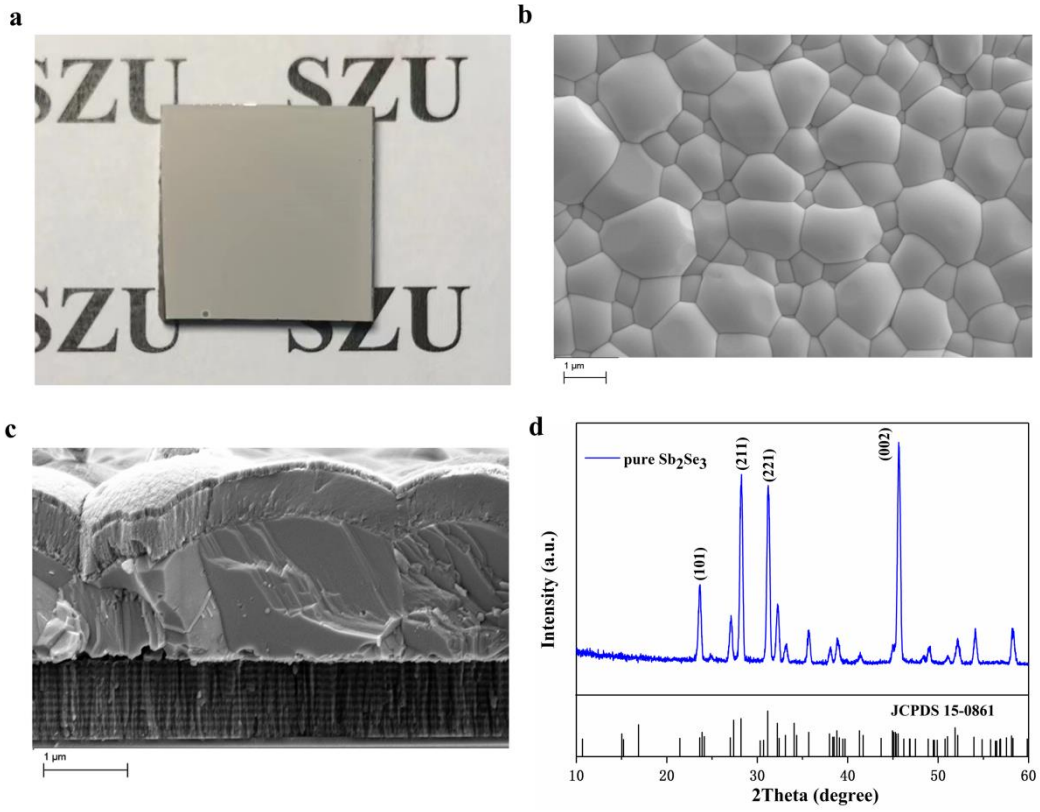

Supplementary Figure S1. Morphology of Sb_2Se_3 thin film, **a** photo of the as-prepared Sb_2Se_3 thin film. **b, c** SEM top-view and cross-sectional images of Sb_2Se_3 thin film. **d** XRD spectrum of Sb_2Se_3 thin film.

Supplementary Note 2

In order to evaluate the reproducibility of the device fabrication and the HTJ annealing process, over 50 devices were tested for each sample category and the results are shown in Supplementary Figure S2. The champion device was stored in air ambient without any intentional encapsulation for 60 days. The device presented an excellent stability as the overall PCE barely decreased throughout the whole testing period (Supplementary Figure S3a). *J-V* measurements were also carried out for the champion device using different scanning directions (Supplementary Figure S3b). Apparently, the device displayed no efficiency hysteresis.

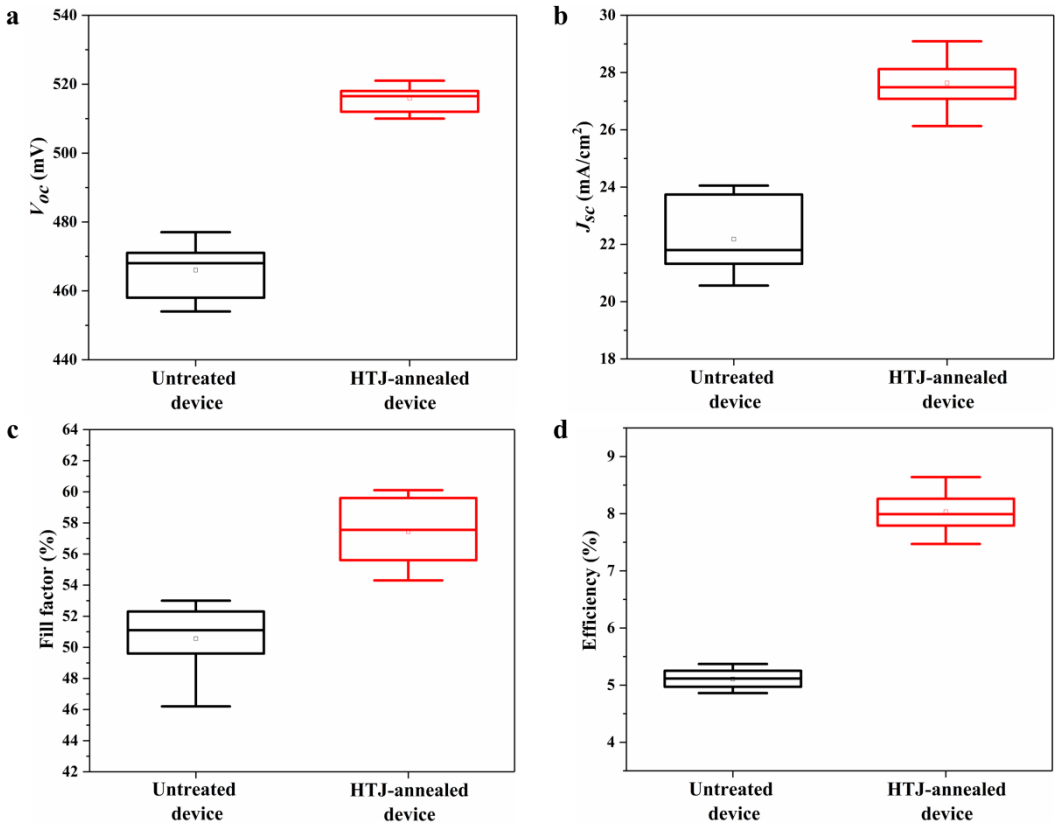

Supplementary Figure S2. Main parameters of the untreated and HTJ-annealed devices.

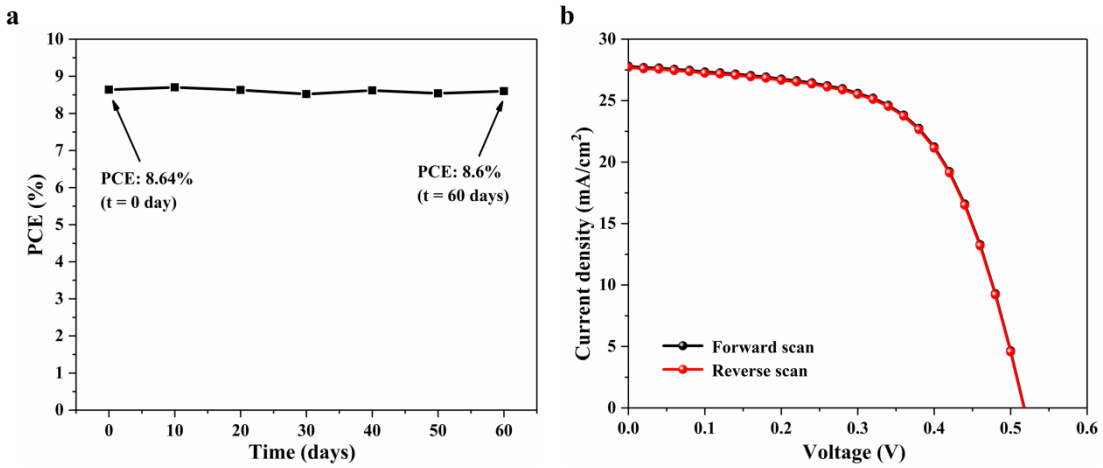

Supplementary Figure S3. a PCE evolution of the champion device after 60 days storage in air ambient without special encapsulation, **b** *J-V* hysteresis behaviour of the champion device.

Supplementary Note 3: **TEM characterization**

Supplementary Figure S4 presents the one-dimensional crystal structure of Sb_2Se_3, where the Sb and Se atoms could be readily distinguished from each other. Five atomic columns C1-C5 are also demonstrated in the figure. In C1 and C2 columns, Sb atoms are located underneath Se atoms, and in C4 and C5 columns the Sb atoms are located above Se atoms, whilst the C3 column is occupied by only one Se atom. Since the intensity of the HAADF signal is known to be proportional to the average Z^2 of each atomic column that behaves as a scattering center, the intensity of columns that contain both Sb and Se atoms should be identical regardless of the atom position. This is consistent with the intensity profile data displayed in Figure 3d for the untreated device, as a result only C1 is selected as representative for atomic columns contain both Sb and Se atoms in the main text. Also, given that the atomic number of Sb (51) is much larger than that of Se (34), the C1 columns would always appear as 'bright dots' in the HAADF-STEM image. On the other hand, the C3 columns which contain only one Se atom, would appear as 'dark dots.

The original HAADF-STEM image was poorly resolved, leading to a very noisy intensity profile obtained from the image (Supplementary Figure S5a). In order to improve the image quality, the raw image was Gaussian blur processed after which the atomic columns became clearly resolved. As a result, the Sb substitution by Cd for the HTJ annealed device can be readily observed in the intensity profile derived from the processed image, as shown in Supplementary Figure S5b.

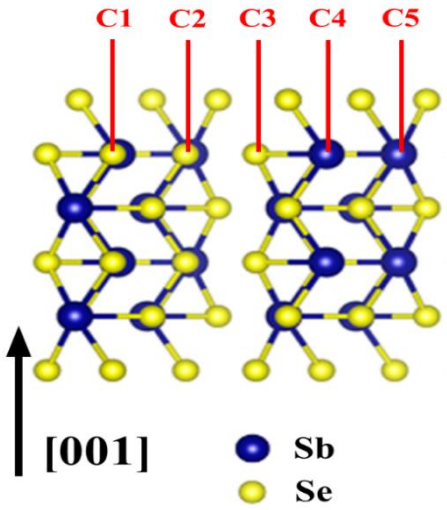

Supplementary Figure S4. Crystal structure of Sb_2Se_3.

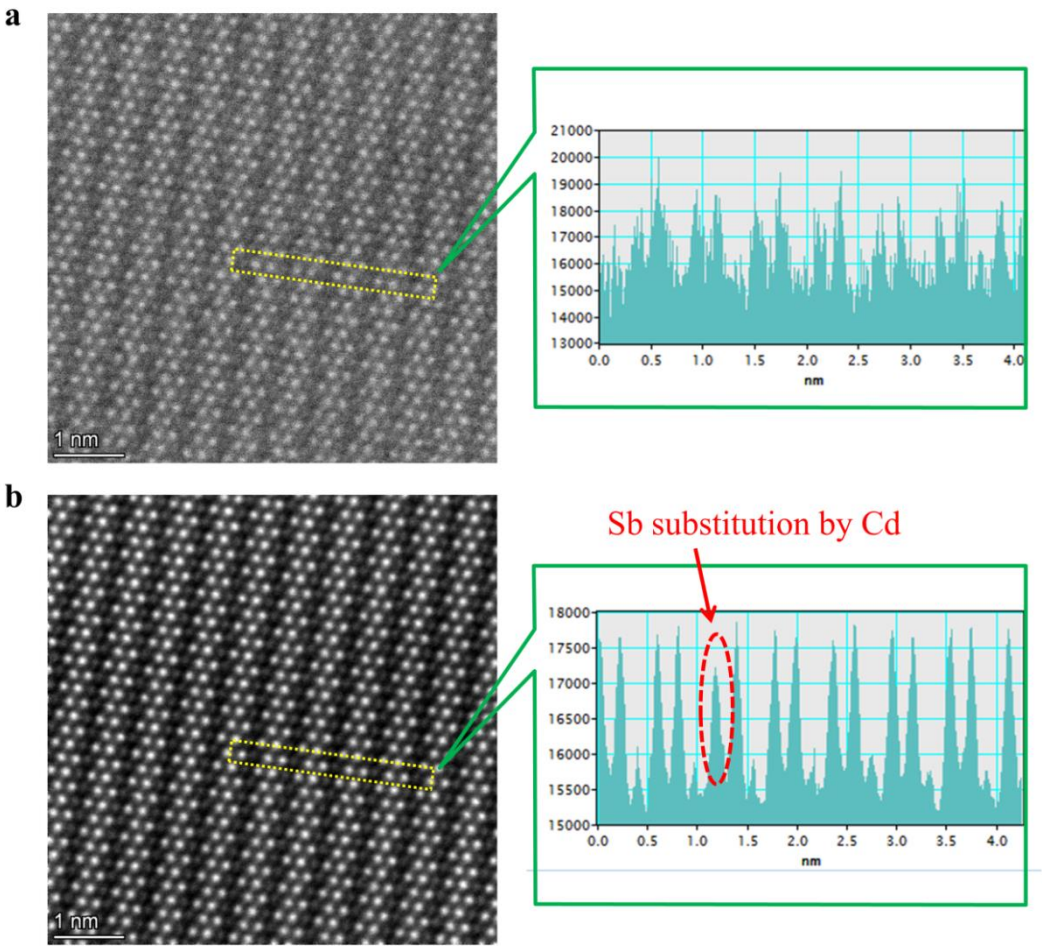

Supplementary Figure S5. HAADF-STEM images before and after Gaussian blur processing**. a** Original image, **b** Gaussian blur processed image.

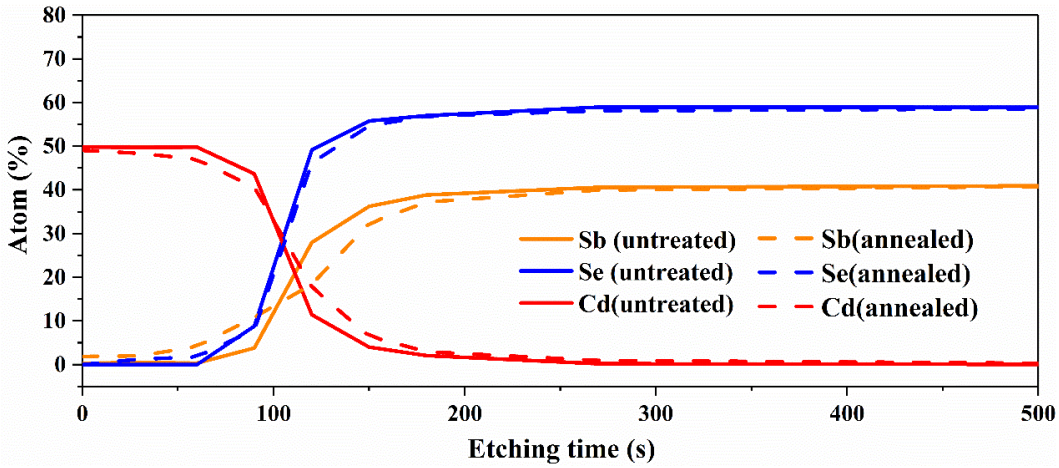

Supplementary Figure S6. XPS elemental depth profiles across HTJ regions of the two devices.

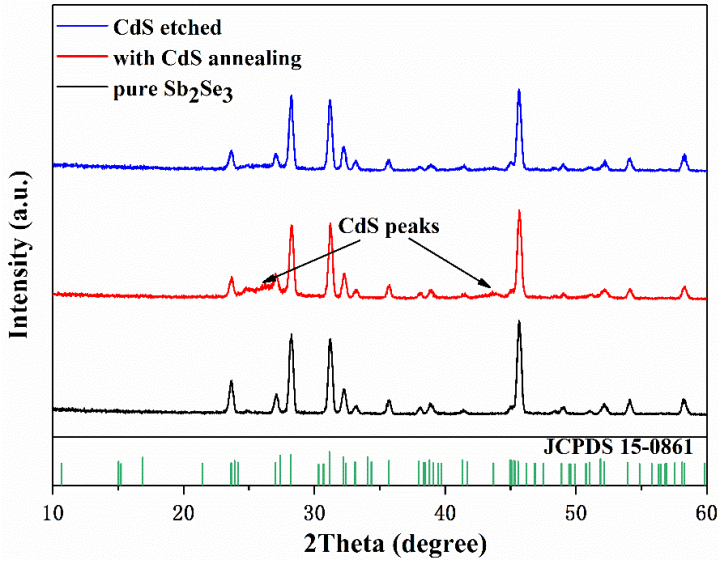

Supplementary Figure S7. XRD patterns of the pure Sb_2Se_3 thin film, the as-annealed Sb_2Se_3/CdS composite and the Sb_2Se_3 thin film after CdS etching.

Supplementary Table S1. Summary of the *C-V* and *DLCP* results of the two devices.

Device	N_{CV} (cm^{-3})	N_{DLCP} (cm^{-3})	W_d (nm)	N_i (cm^{-3})
Untreated	9.52×10^{14}	2.27×10^{14}	320	7.25×10^{14}
Annealed	1.71×10^{15}	1.32×10^{15}	199	3.9×10^{14}

Supplementary Note 4

Ultraviolet photoelectron spectroscopy (UPS) was performed to determine valence and conduction band positions as well as Fermi levels for the untreated and HTJ-annealed Sb_2Se_3 thin films, the results are provided in Supplementary Figure S8 (for the HTJ-annealed sample, the CdS buffer layer was etched away from the top of Sb_2Se_3 film using low-concentration HCl before test). Both Sb_2Se_3 absorber thin films are confirmed to be p-type semiconductors.

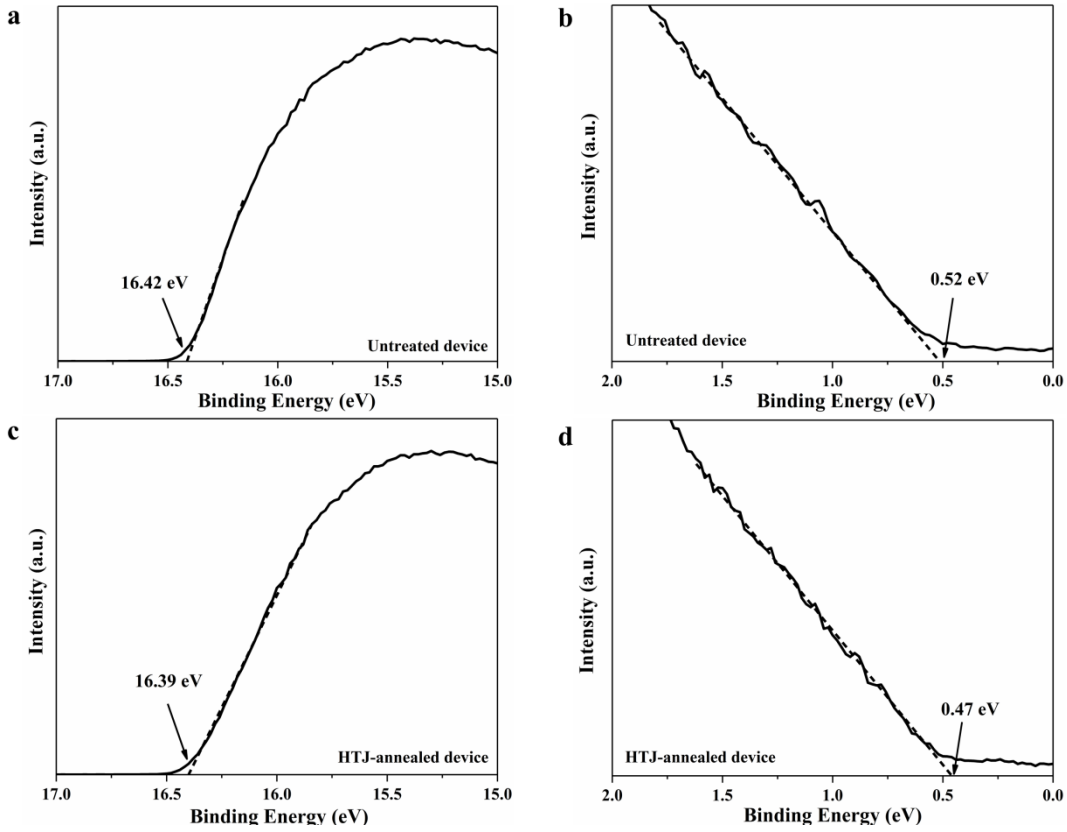

Supplementary Figure S8. UPS characterization of Sb_2Se_3 thin films. **a, b** Secondary electron cutoff and valance band of the untreated Sb_2Se_3 thin film. **c, d** Secondary electron cutoff and valance band of the HTJ-annealed Sb_2Se_3 thin film.

Supplementary Table S2. Summary of carrier lifetimes of the two devices. The average lifetime τ is calcultated according to the equation: $\tau = (A_1\tau_1^2 + A_2\tau_2^2)/(A_1\tau_1 + A_2\tau_2)$.

Device	A_1	τ_1 (ps)	A_2	τ_2 (ps)	τ (ps)
Untreated	42.86%	110	57.14%	880	814
Annealed	21%	234	79%	5721	5662